BIOCHEMISTRY
including biophysical chemistry & molecular biology

Article

pubs.acs.org/biochemistry

Catalytic Mechanism of Mammalian Adenylyl Cyclase: A Computational Investigation

David K. Hahn, Jose R. Tusell, Stephen R. Sprang, and Xi Chu*

Center for Biomolecular Structure and Dynamics and Department of Chemistry and Biochemistry, The University of Montana, Missoula, Montana 59812, United States

Supporting Information

ABSTRACT: Adenylyl cyclase (AC) catalyzes the synthesis of cyclic AMP, an important intracellular regulatory molecule, from ATP. We propose a catalytic mechanism for class III mammalian AC based on density functional theory calculations. We employ a model of the AC active site derived from a crystal structure of mammalian AC activated by G_{α}·GTP and forskolin at separate allosteric sites. We compared the calculated activation free energies for 13 possible reaction sequences involving proton transfer, nucleophilic attack, and elimination of pyrophosphate. The proposed most probable mechanism is initiated by deprotonation of 3′OH and water-mediated transfer of the 3′H to the γ-phosphate. Proton transfer is followed by changes in coordination of the two magnesium ion cofactors and changes in the conformation of ATP to enhance the role of 3′O as a nucleophile and to bring 3′O close to P_{α}. The subsequent phosphoryl transfer step is concerted and rate-limiting. Comparison of the enzyme-catalyzed and nonenzymatic reactions reveals that the active site residues lower the free energy barrier for both phosphoryl transfer and proton transfer and significantly shift the proton transfer equilibrium. Calculations for mutants K1065A and R1029A demonstrate that K1065 plays a significant role in shifting the proton transfer equilibrium, whereas R1029 is important for making the transition state of concerted phosphoryl transfer tight rather than loose.

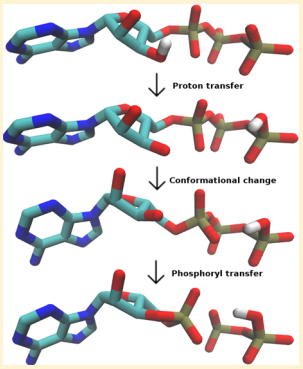

By catalyzing the synthesis of 2′,3′-cyclic AMP (cAMP) from ATP, adenylyl cyclases (ACs) play vital and diverse roles throughout all kingdoms of life. In mammals, cAMP is a universal second messenger that controls cellular processes, including metabolism, secretion, and gene transcription.[1,2] Mammalian type V cyclases are implicated in cardiac function, and there is interest in these enzymes as therapeutic targets.[3] Mammalian ACs belong to the class III family of nucleotidyl cyclases.[2,4] The catalytic cores of class III cyclases are composed of two homologous or identical "cyclase homology domains" (CHD), assembled about a two-fold or quasi-two-fold axis of symmetry.

Mammalian class III cyclases, of which 10 isoforms have been identified, contain two distinct CHDs within a single polypeptide chain (named C1 and C2, the N- and C-terminal CHDs, respectively). The catalytic site is located at the interface between the C1 and C2 domains. The C1 and C2 domains have similar tertiary structures, but because their amino acid sequences have diverged, there is only one functional catalytic site. The second, pseudodyad-related site may serve a regulatory function.[5,6]

Adenylyl cyclase converts ATP to cAMP in a reaction that proceeds by direct displacement of pyrophosphate by in-line attack of the ribosyl 3′OH on the α-phosphate, with inversion of configuration, and without formation of a covalent enzyme-bound intermediate.[7] The forward reaction requires Mg^{2+}-ATP and free Mg^{2+} as an enzyme cofactor.[8] Models for the catalytic core of class III ACs are provided by a series of crystal structures of the complex between the C1 domain of type V and the C2 domain of type II AC (VC1:IIC2) bound to a variety of ATP analogues and substrate-based inhibitors[9−11] and complexes of soluble, bicarbonate-regulated ACs.[12,13] These structures, together with mutagenic and biochemical analyses (e.g., refs 9, 14, and 15), have revealed the protein residues responsible for nucleotide binding and catalysis and elucidated the mechanisms by which AC activity is regulated.

Crystal structures of adenylyl cyclase bound to ATP analogues[9,10,12,13] reveal two metal cofactors in its active site, similar to binuclear metalloenzymes that catalyze phosphoryl transfer and DNA or RNA polymerization.[16−22] Mammalian class III enzymes utilize both Mg^{2+} and Mn^{2+} as metal cofactors, although it is most probable that Mg^{2+} is the physiologically relevant species. These cofactors are thought to play crucial roles during enzyme catalysis. It is proposed that one of the two ions, metal A (Figure 1), interacts with the ribosyl 3′OH to facilitate proton abstraction and to stabilize the developing charge on the 3′O during nucleophilic attack. A second metal ion bound at site B binds the negatively charged triphosphate moiety of ATP and stabilizes the products cAMP and pyrophosphate (PP_i) in the binding site.[16] Two aspartates (residues 396 and 440 in type V adenylyl cyclase) form bidentate ligands of both metal ions and are universally conserved among class III ACs.[2]

Received: June 12, 2015
Revised: September 15, 2015
Published: September 22, 2015

DOI: 10.1021/acs.biochem.5b00655
Biochemistry 2015, 54, 6252−6262

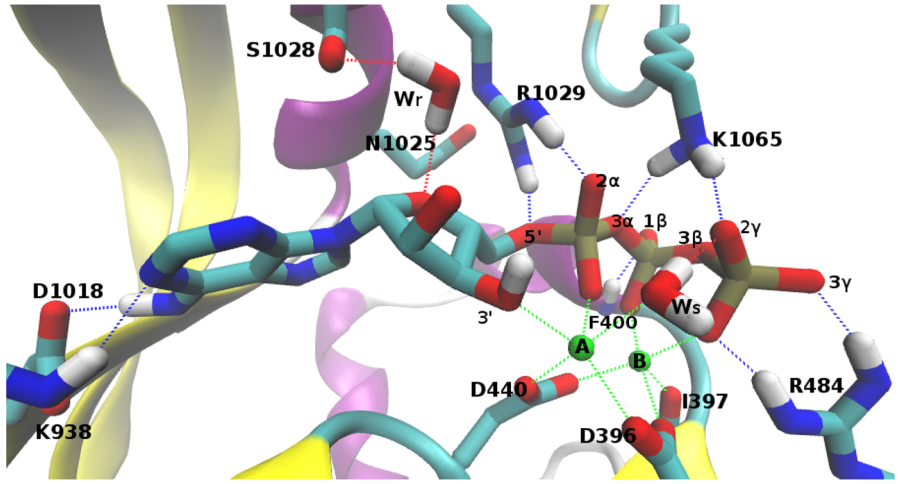

Figure 1. Conformation of the AC·ATP complex **R**. Coordination bonds are shown as green dashed lines and hydrogen bonds as red (donor is oxygen) or blue (donor is nitrogen) dashed lines. The secondary structure of AC is from the crystal structure (Protein Data Bank entry 1CJK). Yellow for C1 and purple for C2. The only hydrogen atoms shown are the O3′H, those that form hydrogen bonds, and those that belong to water molecules W_r and W_s.

Crystal structures provide useful starting points from which to model end points and intermediate states of the cyclization reaction but suffer from significant limitations. Structural studies have thus far focused on complexes with ATP analogues and P site inhibitors in which the 3′OH is either absent, phosphorylated, or derivatized, or in which the α-phosphate is substituted with a thiol. These modifications eliminate or perturb enzyme−metal−substrate interactions that are critical to catalysis. Moreover, in all cases, the ATP α-phosphate is rotated away from the ribose ring, rather than positioned over the 3′OH, as would be required for an in-line attack. It is likely that ligand-field interactions involving the A site metal with the 3′-hydroxyl and the α-phosphate pro-R_p exocyclic oxygens are essential for stabilizing the energetically unfavorable pre-transition state conformation of ATP. Coordinated by the phosphate oxygen atoms of ATP, the metal ions at the active site play a significant role in stabilizing the conformation of ATP.

Here, computational modeling is employed to elucidate the catalytic mechanism of AC. We use an approach established by Siegbahn et al.,[23] which relies on a QM model that focuses on the active site. Because it allows more active site atoms to be treated quantum mechanically, application of this approach has yielded important mechanistic insights.[23,24] This treatment, however, ignores medium- and long-range effects of the enzyme on the active site during the course of the reaction.

Because conformational changes in the ATP substrate are required to align the ribosyl 3′OH with the α-phosphate, it is necessary to include the entire ATP molecule in the model. Consequently, we treat ATP and all residues that form hydrogen bonds with ATP quantum mechanically to ensure a proper description of the conformational changes that occur in the reaction. We adopt the polarizable continuum model (PCM)[25] for the solvent.

We used the QM/PCM model to compare the activation energies for alternative reaction paths. It is a well-characterized approach for examining the relative free energies of intermediates and transition states for various reaction paths. The model incorporates only the subset of the enzyme directly involved in catalysis and substrate binding, and does not sample conformational space. Our calculations therefore ignore the entropic contribution due to the existence of multiple substrate and active site conformations.[26] However, the computational cost of combining QM calculations of this size with conformational sampling is prohibitively large. The errors in solvation energy due to employing PCM may differ significantly from one path to another. Therefore, our selection of the most probable mechanism is based on a limited model, which not only treats the solvation and protein environment at the PCM level but also ignores medium- to long-range effects of the enzyme on the active site and conformational sampling of the enzyme. Within this model, however, the activation free energy differences between the most probable mechanism and the others are substantial, and knowledge of this path will inform future studies of similar systems that include an accurate description of the conformational ensemble, solvation, and allosteric effects.

Wolfenden[27] and Warshel[28] have demonstrated the importance of comparing uncatalyzed and catalyzed reactions in enzymology concerning phosphoryl transfer. Using the QM/PCM model, we calculated reaction free energies for the same mechanism in bulk solvent and as catalyzed by the enzyme. Detailed thermodynamic data are available for protonating ATP in solution, and these provide a check on the accuracy of the method, which is subject to errors that arise from a lack of conformational sampling, the use of PCM, and approximations inherent in DFT. We show that computationally derived free energies are within a few kilocalories of experimentally determined values. Comparisons between the free energies of intermediates and transition states for ATP cyclization in bulk solvent versus that catalyzed by AC provide insight into the roles of active site residues.

By determining the reaction path for the AC-catalyzed cyclization reaction, we address the following questions unique to AC catalysis. (i) What is the sequence of events for nucleophilic attack, elimination, and proton transfer? (ii) Is the reaction associative or dissociative? Is it stepwise or concerted? (iii) What is the base that accepts the ribose 3′-hydrogen? (iv) How does metal coordination evolve during the reaction trajectory? (v) What is the conformation of the product, cAMP, and how is it bound to the active site?

DOI: 10.1021/acs.biochem.5b00655
Biochemistry 2015, 54, 6252−6262

METHODS

We obtained a preliminary model of the AC enzyme−substrate complex from the crystal structure of the mammalian VC1 and IIC2 domains bound to adenosine 5′-(α-thio)-triphosphate (ATPαS-R_p) and $G_{s\alpha}$ [Protein Data Bank (PDB) entry 1CJK], replacing the sulfur with oxygen, and replacing Mn^{2+} at the B site with a physiologically relevant Mg^{2+}. The model consists of all amino acid residues for which at least one non-hydrogen atom is within 3.5 Å of any atom of ATPαS-R_p. Included in the model are two aspartates, D396 and D440, each of which provides a bridging carboxylate for the two metal ions, which in turn restrain the conformation of the ribose and triphosphate moieties; I397, which coordinates metal B; F400, which may form a hydrogen bond with the β-phosphate; three residues, R1029, K1065, and R484, that form ionic interactions with the ATP triphosphate; two residues, D1018 and K938, that form hydrogen bonds with the adenine moiety of ATP; and N1025 and S1028, which interact with the ribosyl moiety. D396, I397, D440, F400, and R484 are residues of the C1 domain, and the other residues are from the C2 domain. Two metals, ATP, and two water molecules present in the crystal structure are also included in the model. One of the water molecules (W_s), which serves as a proton shuttle, is coordinated to Mg_A^{2+} at a distance of 2.6 Å in the crystal structure. The second (W_r) is hydrogen-bonded to the ribose ring oxygen and side chain atoms of Ser1028 and Arg1029 and is within 3.5 Å of the ribose 3′O. The bulk solvent and the protein environment are treated by PCM.

Most of the included protein residues are truncated at the C_α atom, with the exception of I397 and F400, and hydrogen atoms are added to complete the valence of each second row element. Main chain atoms of F400 and those connecting D396 and I397 are included in the model and constrained to their crystal positions. We constructed the model for the enzyme−substrate ground state by restraining each C_α to its crystallographic position. The influence of this restraint was studied by varying the force constant and the position of each C_α. Following an initial geometry optimization, each hydrogen atom added to C_α was restrained. Conditions of neutral pH are assumed; therefore, the lysine, arginine, and aspartate residues were assumed to be charged, and ATP was assigned a charge of −4, giving the system a net charge of +1 over a total of 193 atoms. The model and atomic labeling convention used in this article are shown in Figure 1. Our model for the reaction in aqueous solution consists of ATP, two Mg^{2+} ions, and two water molecules. The total charge is zero.

The root-mean-square deviation (rmsd) for the heavy atoms in the model with respect to the corresponding atoms in the crystal structure (PDB entry 1CJK) is 1.32 Å. In particular, that for ATP compared to ATPαS-R_p in the crystal is 1.48 Å. This reflects the difference between ATP and its analogue. The largest deviation is 3.97 Å for 3′O; the second largest is 3.29 Å for $O_{3\gamma}$, and the third largest is 2.87 Å for $O_{1\gamma}$. Metal A is shifted by 0.470 Å and metal B by 0.271 Å. The shift for 3′O puts it at a better position for nucleophilic attack, and that for $O_{3\gamma}$ and $O_{1\gamma}$ orients $O_{2\gamma}$ to an optimal position to receive a proton.

Starting from the enzyme−substrate complex, we first scanned the potential energy surface along sequences of bond distance or bond angle changes that accompany each of the possible reaction mechanisms. Potential energy curves were thus obtained for several possible reaction paths. These paths exhaust the possible sequences involving three events: nucleophilic attack, elimination of the pyrophosphate, and proton transfer. There are six possible reaction paths if all events are sequential and stepwise. There are seven more possibilities when we consider the situations in which two or three events are concerted. Additional possibilities appear when we consider different proton transfer pathways.

On the basis of results from relaxed potential energy surface scans (with geometry optimization at each point), we first eliminated those paths with barriers that were prohibitively high. Nine of the 13 trajectories we scanned have no maximum in at least one of the reaction steps, and in that step, the energy increases monotonically. The initial point is at an energy minimum, but the ending point is not a stationary point. In mechanism (i), for example, as we scan the nucleophilic attack step, the electronic energy increases as the P_α−3′O distance decreases. We ended the scan at 1.7 Å, because a P_α−3′O bond forms at this distance. The energy at the end point is much larger than 35 kcal/mol, and hence, we conclude that the activation energy of mechanism (i) must be higher than 35 kcal/mol. In Table 1, we record the P_α−$O_{3\alpha}$ and P_α−3′O distances at the end point of the scan. Even though no saddle point is found in the scan, the geometry at the end point

Table 1. P_α−O Distances in RDTS and Free Energy Barriers for Different Mechanisms

	distance in RDTS (Å)[a]		
mechanism	P_α−$O_{3\alpha}$	P_α−3′O	activation free energy (kcal/mol)
(i)	∼1.8[b]	<1.7	>35
(ii)	∼1.8[b]	<1.7	>35
(iii)	>2.4	∼2.5[d]	>50
(iv)	>2.4[c]	<1.7[c]	>35
(v)	∼1.8[b]	<1.7	>35
(vi)	>2.4	∼2.5[d]	>50
(vii)	>2.4	∼2.5[d]	>50
(viii)	>2.4	∼2.2[d]	>50
(ix)	∼2.1	∼2.2	31[e]
(x)	∼1.8	∼1.9	28[e]
(xi)	>2.4	∼2.1[d]	>32
(xii)	1.80	2.07	17.9
(xiii)	∼1.7	∼2.2	27[e]

[a]Note that ∼ indicates that there is no saddle point and the energy keeps increasing while the P_α−$O_{3\alpha}$ or P_α−3′O distance is being varied (see Methods). The distance following ∼corresponds to the structure with the largest energy calculated. [b]The energy increases with decreasing P_α−3′O distance. Geometry optimization was performed after fixing this distance at 1.7 Å, which rendered the P_α−$O_{3\alpha}$ distance. [c]The energy increases with increasing P_α−$O_{3\alpha}$ distance and decreasing P_α−3′O distance. [d]The energy increases with increasing P_α−$O_{3\alpha}$ distance. Geometry optimization was performed after this distance had been fixed at 2.4 Å, which rendered the P_α−3′O distance. [e]The initial search for the saddle point was performed with the 199-atom model and the electronic energy converged to 0.2 kcal/mol. Further optimization required for a subsequent frequency calculation turned out to be extremely time-consuming. Because the electronic energy is more than 10 kcal/mol higher than that of the most probable mechanism, and the entropic contribution of free energy is well within 5 kcal/mol, a smaller model is adopted to finalize the frequency calculations. Because the adenyl ring, D1018, and K938 appear to be fixed in the 199-atom optimization and the difference in their bond distances between the reactant and RDTS is within 0.003 Å, they are excluded in the smaller model with 133 atoms. We approximate $\Delta G \simeq \Delta V_{199} - T\Delta S_{133}$, where 199 and 133 indicate the number of atoms included in the calculation.

DOI: 10.1021/acs.biochem.5b00655
Biochemistry 2015, 54, 6252−6262

reflects the nature of the mechanism: the P_α–$O_{3\alpha}$ and P_α–3′O distances are 1.8 and 1.7 Å, respectively, which indicates that this is an associative path. Mechanisms (i), (ii), and (v) share the same initial step, for which the energy increases monotonically; therefore, the calculations yield the same P–O bond distances and the same estimated activation free energies (Table 1). For mechanisms (iii), (vi), and (vii), in which the initial step is elimination of pyrophosphate, the energy increases monotonically with an increasing P_α–$O_{3\alpha}$ distance. We terminated the scan at 2.4 Å, at which distance the energy is higher than 50 kcal/mol. At this terminal geometry, the P_α–3′O distance is 2.5 Å, and there is no valence bond between the two atoms. In mechanism (xi), elimination is the second, rather than the first, step in the reaction sequence. Mechanisms (iv) and (xi) involve two-dimensional scans. For mechanism (iv), the P_α–$O_{3\alpha}$ and P_α–3′O distances are the scan variables. The energy increases monotonically with an increase in the former and a decrease in the latter. We terminated the scan at 2.4 and 1.7 Å for the P_α–$O_{3\alpha}$ and P_α–3′O distances, respectively, because the P_α–$O_{3\alpha}$ bond is broken and the P_α–3′O bond formed at those distances. For mechanism (xi), the scan variables are the P_α–$O_{3\alpha}$ and H_{w_s}–$O_{2\gamma}$ distances. The energy increases monotonically with the P_α–$O_{3\alpha}$ distance, and we terminated the scan at 2.4 Å.

For the remaining paths, i.e., mechanisms (ix), (x), (xii), and (xiii), we calculated energies for the full reaction trajectory. From the maxima of the selected potential curves, we searched for first-order saddle points to obtain the transition states. From each first-order saddle point, the adjacent local minimum at either side of the transition state was obtained by using the intrinsic reaction coordinate method[29] to find the intermediates. Connecting the intermediates and transition states, we obtained complete reaction paths from the reactant to the products. The free energy barrier or activation free energy, $\Delta G^{\ddagger}_{AC\cdot ATP}$, of the reaction is calculated as the difference between the highest transition state and the ground state. This free energy difference refers to enzyme-bound states of the reactants and products, not to ΔG° for the reaction in solution. The path with the lowest energy barrier is considered the most probable. Stationary points, including both the minima and the saddle points, were calculated in Cartesian coordinates using analytical gradient techniques. The Hessian and free energy of each stationary point were determined by a normal coordinate analysis.

The first-order saddle point calculations were extremely time-consuming. To accelerate the calculation, we initially set the convergence parameter for the electronic energy to be 0.2 kcal/mol. Such a loose convergence, however, cannot be followed by a frequency calcuation. To achieve tighter convergence, we reduced the 199-atom model to a 133-atom model by eliminating the adenyl ring, D1018, and K938, because they appear to be fixed in the 199-atom optimizations. The difference in their bond distances between the reactant and RDTS is within 0.003 Å. A larger difference occurs in the torsion angles relative to the ribose, which does not have much influence over the frequency calculation. Therefore, we approximate $\Delta G \simeq \Delta V_{199} - T\Delta S_{133}$, where 199 and 133 indicate the number of atoms included in the calculation. We adopted this approximation for mechanisms (ix), (x), and (xiii). For mechanism (xii), because its activation free energy appears to be much lower, we further conducted frequency calculation using the 199-atom model, i.e., $\Delta G \simeq \Delta V_{199} - T\Delta S_{199}$. The difference between the two approximations is within 1.4 kcal/mol, as far as free energies are concerned.

We performed the relaxed potential energy scans, saddle points, and intrinsic reaction coordinate calculations using density functional theory (DFT). We employed the meta-hybrid M06 exchange-correlation functional developed by Zhao and Truhlar.[30] This functional has been recommended for application to organometallic and inorganometallic thermochemistry, over the popular B3LYP functional,[31,32] based on benchmark calculations of thermochemistry, barrier heights, noncovalent interaction energies, and electronic spectra for compounds containing both main group elements and transition metals. Metal–ligand bond energies were part of the benchmark, and Mg^{2+}, which plays an important role in catalysis, was explicitly included.[33] We adopted the 6-31G* basis set[34] and the PCM for bulk solvent. A frequency calculation was conducted at each optimized geometry, and thermodynamic quantities were calculated. All calculations were performed with Gaussian 09.[35]

To verify the consistency between our DFT-derived model for the enzyme–substrate complex and the crystal structures on which it is based, we compared the calculated and experimental metal B–oxygen/sulfur distances, because the metals play significant catalytic roles and the Mg_B^{2+}–O distances are not much affected by the replacement of ATP analogues with ATP. Crystal structures have been determined for AC VC1:IIC2 domains bound to ATP analogues ATPαS-R_p (PDB entry 1CJK) and β-L-2′,3′-dideoxyadenosine 5′-triphosphate (βLddATP) (PDB entries 1CJT and 1CJU) (see the Supporting Information). The rmsd between calculated and crystallographically determined metal–oxygen distances for the βLddATP complex is 0.097 Å, where Mg^{2+} occupies the B site, and 0.13 Å, where the B site is occupied by Mn^{2+}. In both instances, the distances are within the estimated range of uncertainty of 0.2–0.3 Å expected for a 2.8 Å crystal structure.[10]

Using the Eyring equation for a Michaelis–Menten mechanism in which conversion of the enzyme–substrate complex to products is rate-limiting

$$\Delta G^{\ddagger}_{AC\cdot ATP} = -RT \ln \frac{hk_{cat}}{k_B T} \quad (1)$$

where k_B is Boltzmann's constant, T is the temperature, and h is Planck's constant, we derive an activation free energy of 15.3 kcal/mol from the rate constant, 59 s^{-1} at 30 °C, for conversion of ATP to cAMP on the enzyme,[14] for comparison to our results.

After the most probable reaction path and its potential and free energy profiles were obtained, we estimated the effects of restraining C_α atoms by moving each C_α toward and away from the center of mass, with a step size of 0.1 Å, and recalculating the potential energies for the enzyme–substrate complex, the rate-determining transition state (RDTS), and the product complex. Using the finite difference method, we calculated the gradient of the activation energies and reaction energies with respect to the positions of the C_α atoms.

Using the methods described above, we also calculated the free energy profile for the most probable reaction path catalyzed by mutants K1065A and R1029A, as well as in bulk aqueous solvent with the two metal ions present at positions that afford interactions with ATP as in models of the enzyme

DOI: 10.1021/acs.biochem.5b00655
Biochemistry 2015, 54, 6252–6262

active site. Comparisons of these results show us whether and how the enzyme accelerates the reaction.

RESULTS AND DISCUSSION

We define three major steps in the ATP cyclization reaction: proton transfer, nucleophilic attack, and elimination of the pyrophosphate. Together they form 13 possible sequences (see the Supporting Information). Starting from the initial geometry of the enzyme−substrate complex, we performed potential energy scans for each sequence. In this section, we present the most probable reaction sequence and compare it to the others.

We obtained the conformation of ATP in the enzyme−substrate complex **R** (Figure 1). Ligands of Mg_A^{2+} include oxygen atoms from D396, D440, the α-phosphate of ATP, a water molecule, W_s, and the ribosyl 3′O. Coordinated by oxygen atoms from the β- and γ-phosphates, Mg_B^{2+} is crucial for stabilizing the conformation of the triphosphate moiety. Mg_B^{2+} is also coordinated by carboxylate oxygen atoms of D396 and D440 and the carbonyl oxygen of I397. Coordination of Mg_B^{2+} is square bipyramidal with one oxygen atom missing at a basal position: the distance between Mg_B^{2+} and $O_{1\alpha}$, the nearest oxygen atom of the α-phosphate, is 2.68 Å, too large for a coordination bond. Oxygen atoms of the β-phosphate and D396 occupy the axial positions.

Potential and free energy profiles for the calculated most probable reaction path are shown in Figure 2. In this figure, **R** and **P** are the enzyme−substrate and enzyme−product complexes, respectively. **T1**−**T5** are transition states, and **I1**−**I4** are intermediates. The last step of the reaction, a concerted phosphoryl transfer, has the largest activation energy barrier and is rate-limiting. We find that the γ-phosphate is the ultimate acceptor of 3′H and the proton transfer is associated with the second highest barrier. Other steps are changes in metal coordination and in the conformation of ATP, both of which are necessary for phosphoryl transfer.

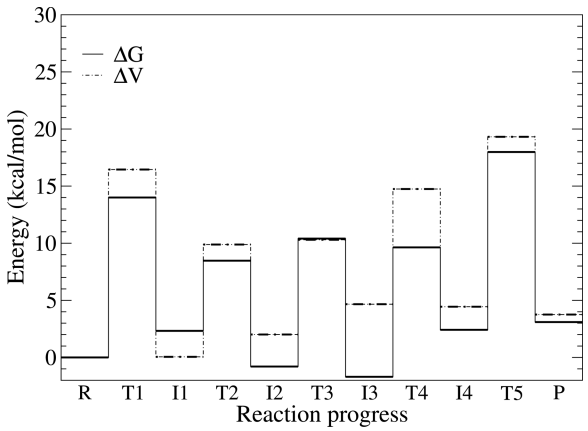

Figure 2. Potential energy, ΔV, and free energy, ΔG, profiles for the most probable path. All stationary points are labeled. Both ΔV and ΔG of **R** are set to zero.

Proton Transfer. In our search for the mechanism with the lowest activation barrier, we sought to answer the following questions: does transfer of O3′H occur prior to, simultaneous with, or after nucleophilic attack? Does it precede or follow elimination of pyrophosphate? Is it assisted by enzyme residues, a water molecule, or the substrate ATP? Potential energy scan calculations indicate that the free energy barriers to nucleophilic attack for mechanisms in which the attack precedes proton transfer are at least 35 kcal/mol. These mechanisms include the following (see the Supporting Information for reaction path schemes): (i) ATP^{4-} → pentavalent intermediate → proton transfer pentavalent intermediate → $cAMP^-$ + PP_i^{3-}, (ii) ATP^{4-} → pentavalent intermediate → cAMP + PP_i^{4-} → $cAMP^-$ + PP_i^{3-}, (iii) ATP^{4-} → trivalent intermediate → cAMP + PP_i^{4-} → $cAMP^-$ + PP_i^{3-}, (iv) ATP^{4-} → cAMP + PP_i^{4-} → $cAMP^-$ + PP_i^{3-}, and (v) ATP^{4-} → pentavalent intermediate → $cAMP^-$ + PP_i^{3-}. The high barriers in these mechanisms are consistent with 3′OH being a poor nucleophile and a weaker base than H_2O: the pK_a of 3′OH is 12.98[36] and that for water 15.74. Deprotonated $3'O^-$ is a better nucleophile than 3′OH.

In sequences (ii)−(iv) mentioned above, elimination of pyrophosphate occurs prior to transfer of the O3′H. In addition, there are three sequences, in which elimination is the first step and nucleophilic attack is the last step, while proton transfer, alternatively, precedes nucleophilic attack and follows elimination, concurs with the nucleophilic attack, or concurs with the elimination: (vi) ATP^{4-} → trivalent intermediate → proton transfer trivalent intermediate → products, (vii) ATP^{4-} → trivalent intermediate → products, and (viii) ATP^{4-} → proton transfer trivalent intermediate → products. Sequences (vi)−(viii) all have activation energies greater than 50 kcal/mol, because of hydrogen bonds to the phosphate moieties of **R** in the tight binding pocket (Figure 1) that prevent elimination.

We also determined the activation energy for (ix) simultaneous nucleophilic attack, elimination, and proton transfer. For this mechanism, it is necessary to first break the coordination bond between 3′O and metal A. This enhances the nucleophilicity of 3′O and prevents proton abstraction prior to attack. The RDTS for this mechanism has a relative energy higher than that for the most probable route, because 3′OH is a weaker acid and a weaker nucleophile in this mechanism. Also, charged residues K1065 and R1029 optimize charge redistribution better in the most probable route than in this concerted mechanism.

Having ruled out the nine routes described above, we are left with four reaction pathways, all of which have proton transfer as the first step. Our calculations indicate that the dianionic γ-phosphate is the ultimate general base that abstracts the proton from the 3′-ribose hydroxyl, because abstraction by any other proton acceptor confronts a higher barrier. The γ-phosphate is also the proton acceptor in the proposed two-metal ion catalysis mechanisms for phosphorolysis of GTP by Ras,[37] nucleotidyl transfer reactions in RNA polymerase II,[38] and in DNA polymerases IV[39] and T7.[40] In a recent empirical valence bond/molecular mechanics study of anthrax edema factor,[41] the proposed pathway is initiated by metal-assisted transfer of O3′H to the bulk aqueous solution, while $O_{2\gamma}$, the exocyclic oxygen of the γ-phosphate, remains protonated throughout the reaction. As such, the net effect is the same as in our mechanism.

As for what mediates proton transfer, we considered the negatively charged carboxylates of D440 or D396, the α-phosphate, and ordered water molecules. In the reaction path with the lowest barrier, W_s, the water molecule that coordinates metal A, mediates proton transfer. In **R** (Figure 1), Mg_A^{2+} is coordinated by 3′O and plays the important role of polarizing the 3′OH, which leads to abstraction of O3′H and its ultimate transfer to $O_{2\gamma}$. The distance between 3′O and $O_{2\gamma}$ is 5.24 Å, which is too long for a direct proton transfer. However, the oxygen of W_s is positioned between the donor and ultimate acceptor: 2.98 Å from 3′O and 2.84 Å from $O_{2\gamma}$. W_s is therefore

DOI: 10.1021/acs.biochem.5b00655
Biochemistry 2015, 54, 6252−6262

in a good position to function as a proton relay whereby O3′H is transferred to W_s while W_s protonates $O_{2\gamma}$. Thus, in the first step of the reaction, **R** → **I1**, O3′H is transferred to the γ-phosphate. This proton transfer step crosses a free energy barrier of 14.1 kcal/mol (Figure 2) at transition state **T1**, in which O3′H is shared between 3′O and the oxygen of W_s, while a proton of this water is transferred to the γ-phosphate in a concerted reaction (Figure 3).

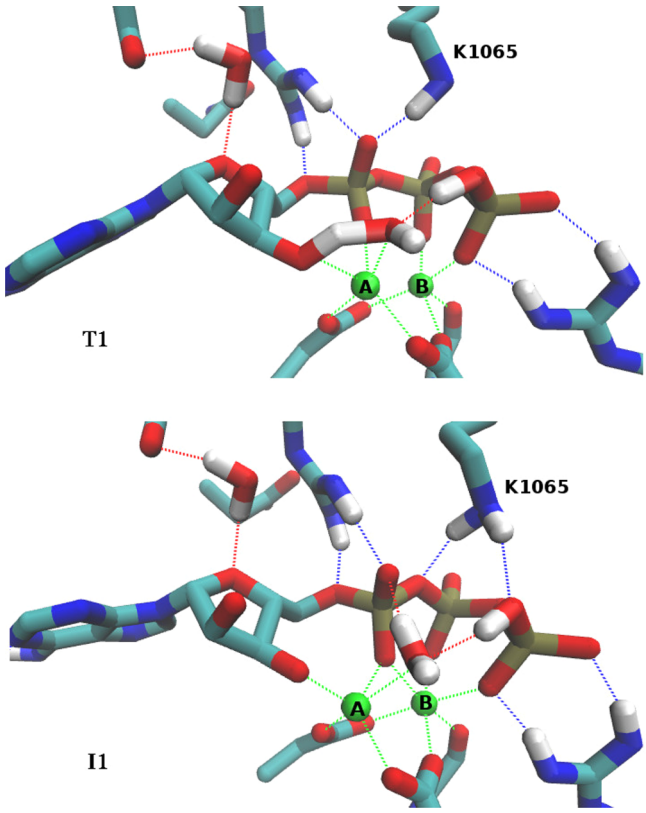

Figure 3. Proton relay transition state **T1** and intermediate **I1**. O3′H is transferred to water molecule W_s, and a proton of W_s is transferred to $O_{2\gamma}$.

The so-called "substrate-assisted" general base catalytic mechanism described above is considered unlikely for non-enzymatic phosphoryl transfer because the proton transfer equilibrium favors protonation of 3′O. Using pK_a values of 12.98 and 6.60 for the ribose 3′O and γ-phosphate, respectively,[36,42] the free energy for proton transfer [$\Delta G_{PT} = \Delta(pK_a)RT \ln 10$] is 8.63 kcal/mol. To compensate for this unfavorable equilibrium, the rate constants for the steps that follow proton transfer would have to be unrealistically large to match the experimental overall rate constant for phosphorolysis.[43] In contrast, our calculations for the enzyme-catalyzed reaction show (Figure 2) that $\Delta G_{PT} = \Delta G_{I1} = 1.60$ kcal/mol, indicating that the equilibrium at the active site is substantially shifted toward **I1**.

The following questions arise. (1) Do the active site residues shift the proton transfer equilibrium? (2) Do the active site residues lower the free energy barrier for proton transfer? To answer these questions, we calculated the relative free energies for the corresponding proton transfer reaction in solution. The system for the solution reaction consisted of ATP^{4-}, two magnesium dications, two water molecules occupying positions corresponding to W_s and W_r, and application of PCM to model bulk solvent. We used the same level of theory and same basis function as in the model for the active site. ΔG_{PT} is calculated to be 9.57 kcal/mol. This is equivalent to a pK_a difference of 7.01, at 298.15 K, between the ribosyl 3′OH and the γ-phosphate, and within 0.63 pK_a unit (0.85 kcal/mol in free energy) of the pK_a difference calculated from the literature values cited above, which is an excellent agreement.

For the reaction in bulk solvent $\Delta V_{PT} = 9.25$ kcal/mol, slightly lower than $\Delta G_{PT} = 9.57$ kcal/mol; however, in the enzyme, $\Delta G_{I1} > \Delta V_{I1}$ (Figure 2), which means that $\Delta S < 0$. The decrease in entropy is consistent with formation of a coordination bond, $O_{1\alpha}$–Mg_B^{2+}, and stronger hydrogen bonds between K1065 and ATP, which help to stabilize **I1** relative to **R** and shift the proton transfer equilibrium toward **I1**. The $O_{1\alpha}$–Mg_B^{2+} distance is 3.00 Å in **R** and 2.22 Å in **I1**, indicating a stronger coordination bond between the two atoms in **I1** (Figure 3).

Even though the electrostatic interaction between Mg_B^{2+} and γ-phosphate is weakened by the proton transfer, that between Mg_A^{2+} and ribose is strengthened by proton transfer. Because the proton acceptor $O_{2\gamma}$ does not coordinate Mg_B^{2+} whereas the proton donor 3′O coordinates Mg_A^{2+}, proton transfer does not weaken the overall metal–substrate interaction. In addition, the new coordination bond formed between $O_{1\alpha}$ and Mg_B^{2+} in **I1** (Figure 3) helps to stabilize this proton transfer intermediate at the AC active site.

The proton transfer step results in a redistribution of charge within the ATP polyphosphate moiety, which is stabilized by structural changes in the side chains of the enzyme residues. In **R**, the tertiary amino group of K1065 forms stronger ionic interactions with the dianionic γ-phosphate than with the α- and β-phosphates (Figure 1). After proton transfer to the γ-phosphate, K1065 moves toward the α-phosphate (Figure 3). The distance between the tertiary amino nitrogen of K1065 and $O_{3\alpha}$ decreases from 3.04 to 2.90 Å, while the distance between the same nitrogen and $O_{2\gamma}$ increases from 2.73 to 2.83 Å.

To further elucidate the role of K1065, we calculated the reaction energy profile for mutant K1065A and found that the ΔG value for **I1** increases by 5.65 kcal/mol. When ATP is in complex with K1065A, the pK_a difference between the ribosyl 3′OH and the γ-phosphate is 5.37 kcal/mol. This value is much closer to the literature value of 12.98 − 6.60 = 6.38 kcal/mol for ATP in aqueous solution, whereas the same pK_a difference we calculated for ATP bound to the wild-type enzyme is 1.18. It demonstrates the significant role of K1065 in shifting the proton transfer equilibrium.

The active site residues reduce the free energy barrier of proton transfer, i.e., the ΔG value for **T1**, by 8.2 kcal/mol relative to the reaction in aqueous solution. For mutant K1065A, this barrier is 3.0 kcal/mol higher that for the wild type. In addition to K1065, calculated structures show that active site residues D396 and D440 play an important role. These residues form bidentate cordination bonds with the two metal ions and anchor them in the active site (Figure 1). The distance between the two ions is 3.32 Å in **R** and 3.36 Å in **T1** (Figure 3). This geometry is critical for water-mediated proton transfer from 3′O to $O_{2\gamma}$. In the bulk solvent model, the two metal ions are separated by 4.02 Å and too far apart to support proton relay, which requires W_s to be within hydrogen bonding distance of both 3′O and $O_{2\gamma}$. To enforce the proton relay in bulk solvent in the transition state equivalent to **T1**, the metal to metal distance must be shortened to 3.52 Å. In the absence of D396 and D440, the Coulomb repulsion between the two

DOI: 10.1021/acs.biochem.5b00655
Biochemistry 2015, 54, 6252–6262

cations sharply increases the relative energy of the transition state in bulk solvent relative to the enzyme active site.

Changes in Metal Coordination and ATP Conformation. To allow intramolecular nucleophilic attack of the ribosyl 3′O on P_α, changes in metal coordination and ATP conformation are necessary. For the most probable mechanism, these changes occur in three steps: **I1** → **I2**, in which the coordination geometry of Mg_A^{2+} changes so that W_s does not hinder P_α from approaching 3′O; **I2** → **I3**, in which the C5′−O5′−P_α−$O_{3\alpha}$ torsion angle changes by −247.2° and the 3′O−P_α distance is shortened by 0.60 Å; and **I3** → **I4**, in which Mg_A^{2+} becomes uncoordinated from 3′O.

The step from **I1** (Figure 3) to **I2** (Figure 4) is mainly a change in Mg_A^{2+} coordination from trigonal bipyramidal to square pyramidal. Water molecule W_s migrates from the axial position of the trigonal bipyramid to a basal position of the square pyramid. This allows 3′O to move closer to P_α. The hydrogen bond between W_s and the γ-phosphate is thus broken, and minor conformational changes in the triphosphate moiety occur. The C5′−O5′−P_α−$O_{3\alpha}$ torsion angle changes from 155° to 143°. K1065 subsequently shifts to form a hydrogen bond with $O_{2\gamma}$.

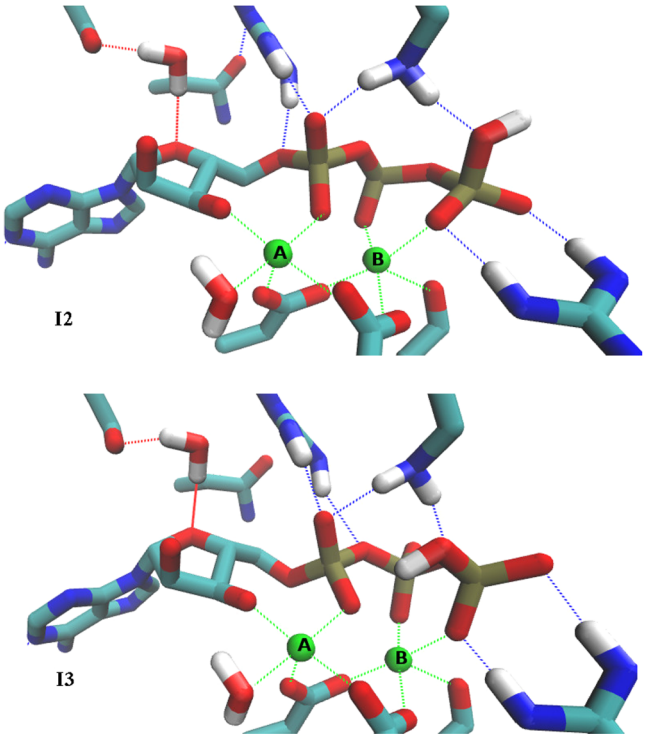

Figure 4. Intermediates **I2** and **I3**, between which changes in metal coordination and ATP conformation, respectively, occur.

During the transition from **I2** to **I3** (Figure 4), the C5′−O5′−P_α−$O_{3\alpha}$ torsion angle changes from 143.4° to −103.8°. This large bond rotation reduces the distance between 3′O and P_α from 3.58 to 2.98 Å, thereby facilitating nucleophilic attack on P_α by 3′O. In addition, the ribose moiety is translated toward S1028. Tracking the rotation about the O5′−P_α bond that repositions the triphosphate moiety, K1065 shifts position to maintain a hydrogen bond with $O_{3\beta}$. This step has a relatively low barrier of 10 kcal/mol because of the hydrogen bonds with R1029 and K1065.

The coordination bond between 3′O and Mg_A^{2+} is broken in the transition from **I3** to **I4**, rendering the former a better nucleophile. Mg_A^{2+} consequently adopts a tetrahedral coordination geometry with the four remaining oxo ligands. As a consequence of translation of the ribose, the W_r-mediated hydrogen bond between S1028 and the ribose 4′O is broken in **I4** (Figure 5). S1028 subsequently forms a hydrogen bond with 2′O, and W_r forms hydrogen bonds with O2′H and $O_{2\alpha}$. R1029 and K1065 shift to form hydrogen bonds with $O_{3\alpha}$ and $O_{2\beta}$. The configuration of hydrogen bonds in **I4** involving ATP with S1028, R1029, K1065, and W_s helps to align 3′O, P_α, and $O_{3\alpha}$ for phosphoryl transfer. Notably, ∠3′O−P_α−$O_{3\alpha}$ = 158.4°. As such, 3′O is posed for in-line nucleophilic attack (Figure 5). In this prephosphoryl transfer conformation, the P_α−$O_{3\alpha}$ distance is 1.60 Å, and thus, the covalent bond between these atoms, which is broken during phosphoryl transfer, remains intact. Meanwhile, the distance between P_α and the 3′O nucleophile is shortened from 3.67 Å in **R** to 3.30 Å in **I4**. All the steps preceding **I4** reduce the activation energy barrier for subsequent phosphoryl transfer.

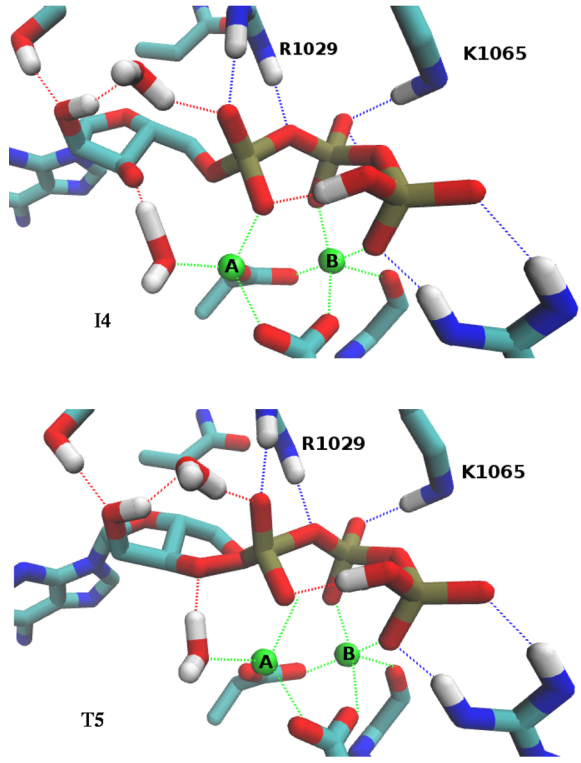

Figure 5. Intermediate **I4** and transition state **T5** for phosphoryl transfer.

The pK_a of 3′O is increased in **I4**, because of breakage of the coordination bond between 3′O and metal A. The pK_a difference between 3′O and $O_{2\gamma}$, however, is increased only slightly to 1.79 for **I4** from 1.18 for **I1**. This is because the pK_a of $O_{2\gamma}$ is also increased substantially because of residue K1065. It breaks the hydrogen bond to $O_{2\gamma}$, which not only causes more negative charge to shift closer to $O_{2\gamma}$ but also allows a conformational change of the γ-phosphate so that a hydrogen bond forms between $OH_{2\gamma}$ and $O_{2\beta}$ (Figure 5).

Phosphoryl Transfer. Following proton transfer, the mechanism of phosphoryl transfer could be (x) stepwise associative, (xi) stepwise dissociative, or (xii) concerted. In

DOI: 10.1021/acs.biochem.5b00655
Biochemistry 2015, 54, 6252−6262

addition, there is a mechanism (xiii) in which formation of a phosphorane intermediate occurs in concert with proton transfer, followed by elimination of pyrophosphate. For mechanisms (xi) and (xii), steps **I1** → **I2** → **I3** → **I4** occur between proton transfer and phosphoryl transfer. For mechanism (x), phosphoryl transfer follows formation of **I3** instead of **I4**. For mechanism (xiii), rotation of the C5′−O5′−P_α−$O_{3\alpha}$ torsion angle occurs first, which results in an intermediate different from the four we discussed. Prior to the concerted proton transfer and nucleophilic attack, 3′O remains coordinated to metal A, whose coordination geometry remains the same as in **R**.

Phosphoryl transfer reactions of phosphate diesters are generally considered to proceed via a concerted mechanism,[44] which is consistent with our findings. Our calculations show that mechanism (xii) has the lowest activation energy. From **I4**, nucleophilic attack of P_α by 3′O and PP_i elimination occur in a single step through the rate-determining transition state (RDTS) **T5**, a pentavalent, or "tight" transition state in which the P_α−3′O and P_α−$O_{3\alpha}$ distances are 2.07 and 1.80 Å, respectively, and ∠3′O−P_α−$O_{3\alpha}$ = 173.6°. The hydrogen bonds between K1065 and $O_{2\beta}$ and between R1029 and $O_{2\alpha}$ in **I4** become stronger in **T5**, and the distances between the corresponding hydrogen donors and acceptors are shortened by 0.081 and 0.06 Å, respectively (Figure 5).

In **P** (Figure 6), the ribose cyclic phosphate of cAMP adopts a twist conformation, with P_α rotated away from the chair

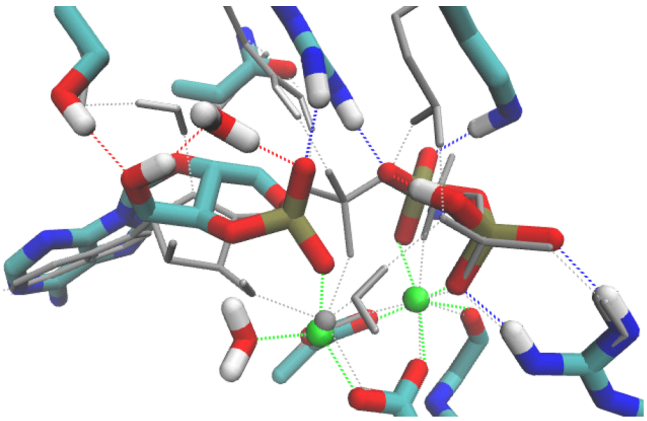

Figure 6. Overlay of product conformation **P** (color) and reactant conformation **R** (gray).

conformation. Restricted by coordination bonds with D396, D440, and the carbonyl oxygen of I397, Mg_A^{2+} and Mg_B^{2+} move by 0.60 and 0.36 Å, respectively, from **R** to **P**. The hydrogen bonds formed by K398 and D1018 with the adenine ring are maintained throughout cyclization. The purine ring rotates 10.2° in the overall transition from **R** to **P**. Hydrogen bonds involving residues S1028, R1029, and K1065 and water W_r formed in **I4** and **T5** are maintained in **P**. These residues, and W_r, form a different constellation of hydrogen bonds in **R**. PP_i is further stabilized by the hydrogen bond between the 2γ proton and the oxygen atom that breaks from the α-phosphate.

Formation of cAMP is mostly achieved by translation of the α-phosphate toward 3′O (Figure 6), as observed in crystal structures of soluble AC.[13] As P_α moves toward 3′O, the bond between P_α and $O_{3\alpha}$ stretches accordingly. In the alternative stepwise dissociative mechanism (xi), elimination involves translation of both the β- and γ-phosphates, which leads to a very high activation energy because the hydrogen bonds among K1065, R1029, and the β- and γ-phosphates cannot be maintained in the transition state for elimination of PP_i.

For the alternative stepwise associative mechanism (x), the RDTS is nucleophilic attack, the free energy of which is substantially higher than that for the elimination step. The entire triphosphate moiety approaches 3′O in this mechanism. Constrained by the moiety's hydrogen bonds with R1029, K1065, and R484 and the coordination bonds with the metal ions, P_α can bind 3′O only if 3′O remains coordinated to Mg_A^{2+}. As such, 3′O is a weaker nucleophile than in the concerted phosphoryl transfer mechanism in which the interaction with Mg_A^{2+} is absent, and hence, the activation energy is higher for the stepwise associative mechanism (Table 1). In mechanism (xiii), nucleophilic attack is concerted with proton transfer. P_α and 3′O are similarly constrained as in mechanism (x), making the activation energy for mechanism (xiii) higher than that for the most probable mechanism (xii) (Table 1).

While Admiraal and Herschlag[45] concluded that ATP hydrolysis involves a dissociative transition state, computational studies of uncatalyzed DNA polymerization, i.e., phosphoryl transfer of phosphate diester rather than monoester, suggested that a concerted mechanism is more probable.[46] We calculated the free energy profile of the cyclization reaction in aqueous solution for a concerted mechanism that incorporates the steps of proton transfer and conformational changes that occur in mechanism (xii) at the active site of mammalian AC. At the transition state for phosphoryl transfer, the P_α−3′O and P_α−$O_{3\alpha}$ distances are 2.06 and 1.87 Å, respectively, similar to those distances at the active site of adenylyl cyclase. The activation energy, however, turns out to be 42.6 kcal/mol, suggesting that the enzyme significantly reduces the activation energy of the reaction. In contrast, on the basis of DFT and Hartree−Fock calculations, Zhang et al. estimated the activation free energy for DNA polarization in solution to be 30.5 kcal/mol.[46] Similar to our results, in their calculated RDTS, the P−O_{nuc} and P−O_{lg} distances are 2.06 and 1.88 Å, respectively. Therefore, even if the transition states are similar, the mechanism of ATP cyclization in solution is likely to be different from that catalyzed at the active site of adenylyl cyclase. Even so, the class III mammalian AC significantly lowers the activation free energy for the concerted mechanism by at least 12.6 kcal/mol and perhaps alters the detailed steps of the reaction relative to that in the aqueous environment. In particular, proton transfer is unlikely to be the first step of the uncatalyzed reaction in aqueous solution

Both the concerted mechanism, as we propose here, and the stepwise associative mechanism have been proposed from computational studies of enzyme-catalyzed two-metal ion-assisted phosphoryl transfer reactions. For example, reactions catalyzed by DNA/RNA polymerases are concerted,[40,47] whereas the anthrax edema factor, a class II adenylyl cyclase, catalyzes a stepwise associative mechanism.[41] The question of why a phosphorane intermediate does not form in class III AC arises. We propose that ion pair hydrogen bonds between R1029 and K1065 and the β-phosphate weaken the P_α−$O_{3\alpha}$ bond as P_α approaches the ribose during nucleophilic attack (Figure 5) and hence favors a concerted phosphoryl transfer.

Mutation of R1029 leads to a >30-fold decrease in AC activity.[48,49] This is consistent with our finding that, for mutant R1029A, the ΔG value of transition state **T5** is 4.11 kcal/mol higher than that of the wild type. In the absence of the

DOI: 10.1021/acs.biochem.5b00655
Biochemistry 2015, 54, 6252−6262

hydrogen bond between R1065 and $O_{3\alpha}$, the energy increases with the $P_\alpha-O_{3\alpha}$ distance, until it is large enough for a hydrogen bond to form between K1065 and $O_{3\alpha}$. So for the transition state of the concerted phosphoryl transfer in R1029A, the $P_\alpha-O_{3\alpha}$ distance is larger than that in the wild type by 1.1 Å. Correspondingly the 3′O−P_α distance is smaller by 0.12 Å. This RDTS in R1029A is therefore "looser" or more "dissociative" than in the wild type.

Sensitivity of the Activation Energy to Active Site Configuration. In the model we computed for the enzyme−substrate complex, **R**, the positions of C_α atoms of all residues restrained to their positions in the 2.8 Å resolution crystal structure[10] of the ATPαS-R_p-bound AC complex (PDB entry 1CJK), which are subject to uncertainties in the range of 0.2−0.3 Å. To estimate the effect of this uncertainty on the activation energy and reaction energy, we calculated derivatives of the potential energies of **R**, **T5**, and **P** with respect to the distance from C_α of each residue to the center of mass of the model (Table 2). The largest derivatives of the activation energy ($\partial\Delta V_{T5}/\partial r_{c_\alpha}$) and reaction energy ($\partial\Delta V_P/\partial r_{c_\alpha}$) are for displacement of I397. The carbonyl oxygen of I397 forms a coordination bond with metal B. Because metal B strongly influences the conformation of the β- and γ-phosphates, the activation energy and reaction energy are sensitive to the position of I397. A shift of the C_α of I397 toward the center of mass by 0.23 Å causes the calculated activation energy to reproduce the value of 15.3 kcal/mol derived from enzyme kinetics.[14] This shift also reduces the calculated free energy difference between enzyme-bound reactants and products to 0.24 kcal/mol, compared with −1.0 kcal/mol derived from enzyme kinetics.[14]

Table 2. Gradient of the Free Energies Relative to the Michaelis Complex with Respect to the Position of the C_α Atoms of Active Site Residues (in kilocalories per mole per angstrom)[a]

residue	$\partial V_R/\partial r_{c_\alpha}$	$\partial V_{T5}/\partial r_{c_\alpha}$	$\partial V_P/\partial r_{c_\alpha}$	$\partial\Delta V_{T5}/\partial r_{c_\alpha}$	$\partial\Delta V_P/\partial r_{c_\alpha}$
D396	−0.487	−0.575	1.53	−0.0881	2.01
I397	−4.23	6.89	7.76	11.1	12.0
D440	3.68	0.734	0.587	−2.95	−3.10
R484	−2.10	−2.12	−2.77	−0.0197	−0.666
K938	2.54	0.274	−0.118	−2.27	−2.66
D1018	4.18	3.56	2.74	−0.624	−1.44
N1025	1.70	−2.69	−1.95	−4.39	−3.65
S1028	0.993	8.02	3.34	7.02	2.35
R1029	−5.93	−5.99	−0.929	−0.0670	5.00
K1065	−3.79	1.08	1.91	4.87	5.70

[a] r_{c_α} is the distance between the α-carbon and the center of the mass of the entire system.

While $\partial\Delta V_{T5}/\partial r_{c_\alpha} = \partial V_{T5}/\partial r_{c_\alpha} - \partial V_R/\partial r_{c_\alpha}$ and $\partial\Delta V_P/\partial r_{c_\alpha} = \partial V_P/\partial r_{c_\alpha} - \partial V_R/\partial r_{c_\alpha}$, values of $\partial V_{T5}/\partial r_{c_\alpha}$ and $\partial V_P/\partial r_{c_\alpha}$ indicate how much the motion of the main chain, which we ignored, affects the activation energy and reaction energy, respectively. For the activation energy, the largest value of $\partial V_{T5}/\partial r_{c_\alpha}$ is for S1028, which forms a hydrogen bond with 2′O in **T5** (Figure 5). Movement of the C_α atom of S1028 toward the center of mass by 0.324 Å in **T5** but not in **R** would allow the conformation of the ribose to be further optimized and thus reduce the activation energy to 15.3 kcal/mol. The second largest is for I397, which we discussed above. The third is for R1029, which is important for the conformation of the phosphates. Moving its C_α away from the center of mass by 0.3 Å in **T5** but not in **R** reduces the activation energy by 1.8 kcal/mol.

CONCLUSIONS

We have formulated an active site model for the mammalian class III AC, which we have used to describe the potential surface along the reaction trajectory for enzyme-catalyzed conversion of ATP to cAMP at the DFT level, at the expense of ignoring the dynamics of the rest of the enzyme and entropic contribution from different conformations. Among 13 possible mechanisms, the reaction sequence with concerted phosphoryl transfer following proton transfer from the ribose to the γ-phosphate has the lowest activation energy.

The measured turnover frequency for conversion of ATP to cAMP on the enzyme is 59 s^{-1} for the forward reaction,[14] from which we estimate that $\Delta G^{\ddagger}_{AC\cdot ATP}$ = 15.3 kcal/mol. From our calculation ΔG_{T5} = 17.9 kcal/mol for RDTS **T5**, which is greater than the experimentally determined value by 2.6 kcal/mol. The rate for the reverse reaction is estimated to be 2.6 s^{-1},[14] from which the free energy of reaction is derived to be −1.0 kcal/mol. The calculated value is 3.1 kcal/mol. The uncertainty of the residue positions in the crystal structure, on which our model is based, and the dynamics of active site that we ignored in the modeling could account for the difference between our results and measurements.

Residues K1065, D396, and D440 facilitate proton transfer from the ribosyl 3′O to the γ-phosphate $O_{2\gamma}$ by decreasing the difference in the pK_a values of the proton donor and acceptor and by anchoring the metal ions and hence reducing the free energy barrier for the proton transfer. Residue R1029 ensures that the transition state for the concerted phosphoryl transfer is "tight".

ASSOCIATED CONTENT

Supporting Information

The Supporting Information is available free of charge on the ACS Publications website at DOI: 10.1021/acs.biochem.5b00655.

Metal−oxygen distances used in benchmark calculation (Table S1), reaction mechanisms we explored (Figures S1−S13), information about the intermediates and transition states of the most probable mechanism (Tables S2−S4), and results for the same mechanism in aqueous solution (Figure S14 and Tables S5−S7) (PDF)

AUTHOR INFORMATION

Corresponding Author

*E-mail: xi.chu@mso.umt.edu.

Funding

The project described was supported by National Institute of General Medical Sciences Grant P20GM103546, National Science Foundation Grant PHY-1506441, and computing time from XSEDE allocations (TG-MCB120042 and TG-MCB120103).

Notes

The authors declare no competing financial interest.

DOI: 10.1021/acs.biochem.5b00655
Biochemistry 2015, 54, 6252−6262

■ ACKNOWLEDGMENTS

We acknowledge helpful discussions with Dr. Valeriy Smirnov.

■ REFERENCES

(1) Sunahara, R., Dessauer, C., and Gilman, A. (1996) Complexity and Diversity of Mammalian Adenylyl Cyclases. *Annu. Rev. Pharmacol. Toxicol. 36*, 461−480.
(2) Sinha, S. C., and Sprang, S. R. (2006) Structures, mechanism, regulation and evolution of class III nucleotidyl cyclases. *Rev. Physiol. Biochem. and Pharmacol. 157*, 105−140.
(3) Watts, V. J. (2007) Adenylyl cyclase isoforms as novel therapeutic targets: an exciting example of excitotoxicity Mol. *Mol. Interventions 7*, 70−73.
(4) Danchin, A. (1993) Phylogeny of adenylyl cyclases. *Adv. Second Messenger and Phosphoprotein Res. 27*, 109−162.
(5) Linder, J. U., and Schultz, J. E. (2003) The class III adenylyl cyclases: multipurpose signaling modules. *Cell. Signalling 15*, 1081−1089.
(6) Tesmer, J. J., and Sprang, S. R. (1998) The structure, catalytic mechanism and regulation of adenylyl cyclase. *Curr. Opin. Struct. Biol. 8*, 713−719.
(7) Eckstein, F., Romaniuk, P. J., Heideman, W., and Storm, D. R. (1981) Stereochemistry of the mammalian adenylate cyclase reaction. *J. Biol. Chem. 256*, 9118−9120.
(8) Garbers, D. L., and Johnson, R. A. (1975) Metal and metal-ATP interactions with brain and cardiac adenylate cyclases. *J. Biol. Chem. 250*, 8449−56.
(9) Tesmer, J. J. G., Sunahara, R. K., Gilman, A. G., and Sprang, S. R. (1997) Crystal structure of the catalytic domains of adeneylyl cyclase in a complex with $G_s\alpha$·GTPγS. *Science 278*, 1907−1916.
(10) Tesmer, J. J. G., Sunahara, R. K., Johnson, R. A., Gosselin, G., Gilman, A. G., and Sprang, S. R. (1999) Two-Metal-Ion Catalysis in Adenylyl Cyclase. *Science 285*, 756−760.
(11) Tesmer, J. J. G., Dessauer, C. W., Sunahara, R. K., Murray, L. D., Johnson, R. A., Gilman, A. G., and Sprang, S. R. (2000) Molecular basis for P-site inhibition of adenylyl cyclase. *Biochemistry 39*, 14464−14471.
(12) Steegborn, C., Litvin, T. N., Levin, L. R., Buck, J., and Wu, H. (2005) Bicarbonate activation of adenylyl cyclase via promotion of catalytic active site closure aand metal recruitment. *Nat. Struct. Mol. Biol. 12*, 32−37.
(13) Kleinboelting, S., Diaz, A., Moniot, S., van den Heuvel, J., Weyand, M., Levin, L. R., Buck, J., and Steegborn, C. (2014) Crystal structures of human soluble adenylyl cyclase reveal mechanisms of catalysis and of its activation through bicarbonate. *Proc. Natl. Acad. Sci. U. S. A. 111*, 3727−3732.
(14) Dessauer, C. W., and Gilman, A. G. (1997) The catalytic mechanism of adenylyl cyclase. Equilibrium binding and kinetic analysis of P-site inhibition. *J. Biol. Chem. 272*, 27787−27795.
(15) Tang, W.-J., Stanzel, M., and Gilman, A. G. (1995) Truncation and Alanine-Scanning Mutants of Type I Adenylyl Cyclase. *Biochemistry 34*, 14563−14572.
(16) Steitz, T., Smerdon, S., Jäger, J., and Joyce, C. (1994) A Unified Polymerase Mechanism for Nonhomologous DNA and RNA Polymerase. *Science 266*, 2022−2025.
(17) Artymiuk, P., Poirrette, A., Rice, D., and Willett, P. (1997) A polymerase I palm in adenylyl cyclase? *Nature 388*, 33−34.
(18) Ellenberger, T., Doublie, S., Tabor, S., Long, M., and Richardson, C. C. (1998) Crystal structure of a bacteriophage T7 DNA replication complex at 2.2 angstrom resolution. *Nature 391*, 251−258.
(19) Kim, E., and Wyckoff, H. (1991) Reaction mechanism of alkaline phosphatase based on crystal structures: Two-metal ion catalysis. *J. Mol. Biol. 218*, 449−464.
(20) Piccirilli, J., Vyle, J., Caruthers, M. H., and Cech, T. (1993) Metal-Ion catalysis in the tetrahymena ribozyme reaction. *Nature 361*, 85−88.
(21) Besse, L., and Steitz, T. (1991) Structural basis for the 3′-5′ exonuclease activity of Escherichia coli DNA polymerase I: a two metal ion mechanism. *EMBO J.*, 25−33.
(22) Steitz, T. (1993) RNA and RNA dependent DNA polymerases. *Curr. Opin. Struct. Biol. 3*, 31−38.
(23) Siegbahn, P. E. M., and Borowski, T. (2006) Modeling Enzymatic Reactions Involving Transition Metals. *Acc. Chem. Res. 39*, 729−738.
(24) Lopez, X. X., Dejaegere, A., Leclerc, F., York, D. M., and Karplus, M. (2006) Nucleophilic attack on phosphate diesters: a density functional study of in-line reactivity in dianionic, monoanionic, and neutral systems. *J. Phys. Chem. B 110*, 11525−11539.
(25) Radhakrishnan, M. L. (2012) Designing electrostatic interactions in biological systems via charge optimization or combinational approaches: insights and challenges with a continuum electrostatic framework. *Theor. Chem. Acc. 131*, 1252.
(26) Pohorille, A., Jarzynski, C., and Chipot, C. (2010) Good Practices in Free-Energy Calculations. *J. Phys. Chem. B 114*, 10235−10253.
(27) Lad, C., Williams, N. H., and Wolfenden, R. (2003) *Proc. Natl. Acad. Sci. U. S. A. 100*, 5607.
(28) Alkherraz, A., Kamerlin, S. C. L., Feng, G., Sheikh, Q. I., Warshel, A., and Williams, N. H. (2010) *Faraday Discuss. 145*, 281−299.
(29) Fukui, K. (1981) The path of chemical-reactions−The IRC approach. *Acc. Chem. Res. 14*, 363−368.
(30) Zhao, Y., and Truhlar, D. (2008) The M06 suite of density functionals for main group thermochemistry, thermochemical kinetics, noncovalent interactions, excited states, and transition elements: two new functionals and systematic testing of four M06-class functionals and 12 other functionals. *Theor. Chem. Acc. 120*, 215−241.
(31) Henriques, A. M., and Barbosa, A. G. H. (2011) Chemical Bonding and the Equilibrium Composition of Grignard Reagents in Ethereal Solutions. *J. Phys. Chem. A 115*, 12259−12270.
(32) Sumimoto, M., Kawashima, Y., Yokogawa, D., Hori, K., and Fujimoto, H. (2011) Theoretical study on the molecular structures of X-, α-, and β-types of lithium phthalocyanine dimer. *J. Comput. Chem. 32*, 3062−3067.
(33) Schultz, N. E., Zhao, Y., and Truhlar, D. G. (2005) Density Functionals for Inorganometallic and Organometallic Chemistry. *J. Phys. Chem. A 109*, 11127−11143.
(34) Ditchfield, R., Hehre, W. J., and Pople, J. A. (1971) Self-Consistent Molecular-Orbital Methods. IX. An Extended Gaussian-Type Basis for Molecular-Orbital Studies of Organic Molecules. *J. Chem. Phys. 54*, 724−728.
(35) Frisch, M. J., et al. (2009) *Gaussian 09*, revision A.1, Gaussian Inc., Wallingford, CT.
(36) Astrom, H., Limen, E., and Stromberg, R. (2004) Acidity of secondary hydroxyls in ATP and adenosine analogues and the question of a 2′,3′-hydrogen bond in ribonucleosides. *J. Am. Chem. Soc. 126*, 14710−14711.
(37) Schweins, H., Geyer, M., Scheffzek, K., Warshel, A., Kalbitzer, H. R., and Wittinghofer, A. (1995) Substrate-assisted catalysis as a mechanism for GTP hydrolysis of p21as and other GTP-binding proteins. *Nat. Struct. Biol. 2*, 36−44.
(38) Zhang, Y., and Salahub, D. (2012) A theoretical study of the mechanism of the nucleotidyl transfer reaction catalyzed by yeast RNA polymerase II. *Sci. China: Chem. 55*, 1887−1894.
(39) Wang, L., Yu, X., Hu, P., Broyde, S., and Zhang, Y. (2007) A Water-Mediated and Substrate-Assisted Catalytic Mechanism for Sulfolobus solfataricus DNA Polymerase IV. *J. Am. Chem. Soc. 129*, 4731−4737.
(40) Wang, L., Broyde, S., and Zhang, Y. (2009) Polymerase-Tailored Variations in the Water-Mediated and Substrate-Assisted Mechanism for Nucleotidyl Transfer: Insights from a Study of T7 DNA Polymerase. *J. Mol. Biol. 389*, 787−796.
(41) Mones, L., Tang, W.-J., and Florian, J. (2013) Empirical Valence Vond simulations of the Chemical Mechanism of ATP to cAMP Conversion by Anthrax Edema Factor. *Biochemistry 52*, 2672−2682.

DOI: 10.1021/acs.biochem.5b00655
Biochemistry 2015, 54, 6252−6262

(42) Rimai, L., Heyde, M. E., and Carew, E. B. (1970) EFFECT OF DIVACENT METAL ION BINDING ON THE RAMAN SPECTRUM OF ATP IN AQUEOUS OLUTION. *Biochem. Biophys. Res. Commun. 38*, 231−237.
(43) Admiraal, S. J., and Herschlag, D. (2000) The substrate-assisted general base catalysis model for phosphate monoester hydrolysis: evaluation using reactivity comparisons. *J. Am. Chem. Soc. 122*, 2145−2148.
(44) Lassila, J. K., Zalatan, J. G., and Herschlag, D. (2011) Biological Phosphoryl-Transfer Reactions: Understanding Mechanism and Catalysis. *Annu. Rev. Biochem. 80*, 669−702.
(45) Admiraal, S. J., and Herschlag, D. (1995) Mapping the transition state for ATP hydrolysis:implications for enzymatic catalysis. *Chem. Biol. 2*, 729−739.
(46) Zhang, Z., Eloge, J., and Florian, J. (2014) *Biochemistry 53*, 4180−4191.
(47) Carvalho, A. T. P., Fernandes, P. A., and Ramos, M. J. (2011) The Catalytic Mechanism of RNA Polymerase II. *J. Chem. Theory Comput. 7*, 1177−1188.
(48) Yan, S.-Z., Huang, Z.-H., Shaw, R. S., and Tang, W.-J. (1997) The Conserved Asparagine and Arginine Are Essential for Catalysis of Mammalian Adenylyl Cyclase. *J. Biol. Chem. 272*, 12342−12349.
(49) Dessauer, C. W., Scully, T. T., and Gilman, A. G. (1997) Interactions of Forskolin and ATP with the Cytosolic Domains of Mammalian Adenylyl Cyclase. *J. Biol. Chem. 272*, 22272−22277.

DOI: 10.1021/acs.biochem.5b00655
Biochemistry 2015, 54, 6252−6262